Oceanic acidification affects marine carbon pump and triggers extended marine oxygen holes

Matthias Hofmann[a] and Hans-Joachim Schellnhuber[a,b,1]

[a]Potsdam Institute for Climate Impact Research, P.O. Box 601203, 14412 Potsdam, Germany; and [b]Environmental Change Institute and Tyndall Centre, Oxford University, Oxford OX1 3QY, United Kingdom

Contributed by Hans-Joachim Schellnhuber, January 8, 2009 (sent for review November 3, 2008)

Rising atmospheric CO_2 levels will not only drive future global mean temperatures toward values unprecedented during the whole Quaternary but will also lead to massive acidification of sea water. This constitutes by itself an anthropogenic planetary-scale perturbation that could significantly modify oceanic biogeochemical fluxes and severely damage marine biota. As a step toward the quantification of such potential impacts, we present here a simulation-model-based assessment of the respective consequences of a business-as-usual fossil-fuel-burning scenario where a total of 4,075 Petagrams of carbon is released into the atmosphere during the current millennium. In our scenario, the atmospheric pCO_2 level peaks at ≈1,750 μatm in the year 2200 while the sea-surface pH value drops by >0.7 units on global average, inhibiting the growth of marine calcifying organisms. The study focuses on quantifying 3 major concomitant effects. The first one is a significant (climate-stabilizing) negative feedback on rising pCO_2 levels as caused by the attenuation of biogenic calcification. The second one is related to the biological carbon pump. Because mineral ballast, notably $CaCO_3$, is found to play a dominant role in carrying organic matter through the water column, a reduction of its export fluxes weakens the strength of the biological carbon pump. There is, however, a third effect with severe consequences: Because organic matter is oxidized in shallow waters when mineral-ballast fluxes weaken, oxygen holes (hypoxic zones) start to expand considerably in the oceans in our model world—with potentially harmful impacts on a variety of marine ecosystems.

climate change | ocean carbon cycle | ocean carbon sink | tipping points

Assessments of carbon inventories inferred from the World Ocean Circulation Experiment (WOCE) (1, 2) have revealed an amount of ≈118 ± 19 Petagrams of carbon (Pg C), or 48% of all fossil fuel and cement-manufacturing emissions by humans, which has invaded the ocean during the period between the years 1800 and 1994 AD (3). Whereas during preindustrial times, the ocean was nearly in equilibrium with the atmosphere, the current oceanic CO_2 uptake exceeds out-gassing by about 2 Pg C per year, equivalent to 1/3 of our current CO_2 emissions (3).

When CO_2 dissolves in sea water, it reacts with water and forms true carbonic acid (H_2CO_3) that dissociates into bicarbonate (HCO_3^-) and hydrogen ions (H^+), which leads to an increase of pH ("ocean acidification"). The surface ocean pH has dropped from ≈8.2 to 8.1 during the last 100 years (4). The oceanic uptake of CO_2 further leads to a decrease of the carbonate ion (CO_3^{2-}) concentration ($CO_2 + H_2O + CO_3^{2-} \leftrightharpoons 2\ HCO_3^-$) and thus to a decrease in the saturation levels for the $CaCO_3$ minerals calcite and aragonite.

Most of the laboratory and field studies during the past reveal that acidification of sea water will hamper biogenic calcification in marine organisms such as corals (5), coccolithophorides (6–8), and foraminifers (9), even when sea water is supersaturated with respect to calcite. Calcification rates for *Emiliania huxleyi* and *Gephyrocapsa oceanica* were found to have dropped by ≈15% and 45%, respectively, under 750 μatm CO_2. Whereas most previous laboratory studies found a decrease in biogenic calcification rates under elevated CO_2 conditions, a recent study with *E. huxleyi* reveals the opposite (10–12). Following the line of arguments of the majority of studies published within the last decade, we assume a net decline of biogenic calcification rates under high CO_2 conditions on global scale.

Photosynthetic fixation of CO_2 by phytoplankton, the sinking of particulate organic carbon (POC) into the deep ocean and its oxidation maintains a vertical gradient in the concentration of dissolved inorganic carbon (DIC), with higher values at depth and lower values at the surface. This "biological carbon pump" (13) plays a crucial role in setting the atmospheric CO_2 concentrations on a time scale from decades to millennia. In contrast to the growth of the soft tissue of phytoplankton cells via photosynthetic fixation of CO_2 in the euphotic zone, formation of calcareous skeletons results in a release of CO_2 (14, 15). Because global precipitation of calcite as a consequence of acidification will become reduced, less CO_2 is formed by marine calcifying organisms. A reduced calcification provides a negative feedback to rising atmospheric pCO_2 levels (7) and thus contributes to stabilization of the Earth's climate.

Below 1,000 m, a strong correlation between the export fluxes of POC and mineral particles, especially with $CaCO_3$, has been found (16). If the flux of mineral ballast declines, there will be less transport of POC into the deep ocean, entailing a weakening of the biological carbon pump. As a result, the above-mentioned negative "calcification feedback" on rising atmospheric pCO_2 levels is counteracted by the reduced mineral ballast transport ("ballast feedback").

In this study, we present an investigation of the implications of a weakened mineral ballast transport on the marine biogeochemistry owing to rising atmospheric pCO_2 levels by employing the 3-dimensional ocean-atmosphere–sea ice-biogeochemistry model POTSMOM-C (see *Methods*). Although our simulations reveal a relatively weak positive ballast feedback, only partly counteracting the negative calcification feedback, the vertical profiles of the distribution of oxygen and macro nutrients will become altered remarkably. Most notably, water masses at intermediate depth will grow toward more anoxic conditions by the year 3000.

Ballast Model

The effect of mineral ballast on the export of POC in an ecosystem model was first accounted for in ref. 17. This model was extended by distinguishing between different categories of ballast (16), where the total vertical export flux of POC (F_{OC} in units of g of C $m^{-2}y^{-1}$) below the euphotic zone is given by the fraction carried by different minerals plus an independently sinking excess flux (F_{OC}^E):

$$F_{OC} = k_{opal} \cdot F_{opal} + k_{CaCO_3} \cdot F_{CaCO_3} + k_{lith} \cdot F_{lith} + F_{OC}^E \quad [1]$$

Author contributions: M.H. and H.-J.S. designed research; M.H. performed research; M.H. analyzed data; and M.H. and H.-J.S. wrote the paper.

The authors declare no conflict of interest.

Freely available online through the PNAS open access option.

[1]To whom correspondence should be addressed. E-mail: john@pik-potsdam.de.

This article contains supporting information online at www.pnas.org/cgi/content/full/0813384106/DCSupplemental.

The dimensionless carrying coefficients [k_{opal} = 0.026, k_{CaCO_3} = 0.083, and k_{lith} = 0.068 (16)] link the vertically declining mass fluxes of opal (F_{opal} in g SiO_2 $m^{-2}y^{-1}$), $CaCO_3$ (F_{CaCO_3} in g of $CaCO_3$ $m^{-2}y^{-1}$), and lithogenic matter (F_{lith} in g of dust $m^{-2}y^{-1}$) to the export flux of mineral ballasted organic matter. Given an exponentially shaped vertical flux distribution, the e-folding penetration depth of F^{E}_{OC} is set to 250 m, whereas for F_{CaCO_3} and F_{opal}, this quantity is set to 5,000 m and 10,000 m, respectively. For simplicity, lithogenic material is assumed to sink immediately down to the sea floor. The ballast model of (16) has been already successfully implemented in 2 OGCMs (18, 19).

Based on experimental findings (6, 7), a simple parameterization has been proposed (20), linking the carbonate ion concentration ($[CO_3^{2-}]$ in μmol L^{-1}) to the calcification rate R_{CaCO_3}, which was applied throughout this study:

$$R_{CaCO_3} \sim \exp\{0.0083 \cdot ([CO_3^{2-}] - C_0)\}. \quad [2]$$

Here, C_0 is set to 150 μmol L^{-1}. An explicit dependence of R_{CaCO_3} on temperature is not considered. Note that the in situ carbonate ion concentration is related to the saturation state of sea water (Ω_{CaCO_3}) with respect to calcium carbonate ($CaCO_3$) via:

$$\Omega_{CaCO_3} = \frac{[Ca^{+}] \cdot [CO_3^{2-}]}{K_{SP}}. \quad [3]$$

$[Ca^{+}]$ is the in situ concentration of calcium ions and K_{SP} the stoichiometric solubility product (21) for calcite. For simplicity, aragonite was neglected throughout this study. Calcite is stable for $\Omega_{CaCO_3} > 1$ and begins to dissolve when Ω_{CaCO_3} drops below 1 (due to acidification and/or due to high pressure in the deep ocean). Under present-day conditions, the ocean surface is supersaturated with respect to calcite, possessing a global mean value of Ω_{CaCO_3} of ≈5.7.

Numerical Experiments

The model was integrated until reaching a steady state (spin-up of 6,000 years). This steady state is used as initial condition for the calendar year 1800. Integration from 1800 to 2000 is driven by reconstructed CO_2 emission rates (22).

For the future projections, the present study utilizes the IPCC SRES business-as-usual emission path, A1FI, beginning in the year 2000 continuing through 2100 (23) and extending it until 2200 by assuming a linear decline to zero, corresponding to a release of 4,075 Pg C in total. Between the years 2200 and 3000 the CO_2 emission rates have been kept at zero (Fig. 2*A*).

To infer the sensitivity of the marine biogeochemistry with respect to changes in the ballast-bound vertical transport of organic matter, we have carried out 3 different model runs, accompanied by a control run (**CONTROL**). The first experiment (**BALLAST**) employs the full-scale biogeochemistry model (see *Methods*) including the ballast transport equation (Eq. **1**) and the $[CO_3^{2-}]$-dependent calcification rate (Eq. **2**). The second model experiment (**FROZEN_BALL**) deviates from **BALLAST** only in the calcite export flux F_{CaCO_3} entering the ballast flux equation (Eq. **1**), assuming this quantity not to be affected by elevated CO_2 levels. Thus, in experiment **FROZEN_BALL**, the relative amount of POC carried by $CaCO_3$ particles remains frozen at a preindustrial level. The third experiment (**FROZEN_CALC&BALL**) differs from **FROZEN_BALL** only by additionally keeping the CO_3^{2-} concentrations in Eq. **2**—the rate equation for biogenic calcification—unchanged at the preindustrial level. By comparison with **BALLAST**, **FROZEN_BALL** allows us to attribute the net effect of oceanic acidification on the ocean's biogeochemistry and atmospheric pCO_2 levels caused by the modified vertical ballast transport (positive ballast feedback), whereas the difference between **FROZEN_CALC&BALL** and **FROZEN_BALL** permits the quantification of the sole impact of reduced calcification rates (negative calcification feedback).

Results and Discussion

Steady State. At initial steady state (year 1800) the model reveals a maximum strength of the Atlantic Meridional Overturning Circulation (AMOC) of 23 Sv (1 Sv = $10^6 m^3 s^{-1}$), an atmospheric pCO_2 of 282 μatm, a net primary production (NPP) of 43 Pg C y^{-1} (estimates from observations: 35–78 Pg C y^{-1}, ref. 24 and references therein), and an export production (100-m level) of 8.6 Pg C y^{-1}. The calculated number for the POC export is comparable with global estimates from state-of-the-art ocean carbon cycle models (25). It was shown in ref. 26 that state-of-the-art models, based on a realistic ocean circulation provide an export production of POC of between 6 and 13 Pg C y^{-1}

The export of POC is associated with sinking fluxes of biogenic $CaCO_3$ and opal, revealing globally integrated values of 1.2 Pg C y^{-1} and 84.0 Tmol of Si y^{-1}, respectively. Global estimates (27) provide values of $CaCO_3$ export fluxes ranging from 0.5 to 1.8 Pg C y^{-1}, whereas 89–200 Tmol of opal per year are reported to sink out of the euphotic zone. Whereas the modeled steady-state $CaCO_3$ export value lies within the range of literature data, the value for opal appears to be slightly underestimated. However, this slight underestimation will not affect our model results, because opal plays only a minor role for the ballasted vertical transport of POC and does not depend on the atmospheric pCO_2 level. For more details, see Fig. S1.

The model provides a global mean export ratio between $CaCO_3$ and POC (rain ratio) of ≈0.12 mol of C (mol C)$^{-1}$, which is also in line with observation-based estimates between 0.06 ± 0.03 (28) and 0.12 (27). Fig. 1*A* shows the relationship between the calcite saturation state Ω_{CaCO_3} within the upper 100 m and the $CaCO_3$/POC rain ratio for each model grid point. Low values of Ω_{CaCO_3} and $CaCO_3$/POC usually occur in cold waters, whereas high values are typical for the warm tropics.

The vertical flux of POC within the water column can be decomposed into a deep-sinking part, carried by minerals, such as $CaCO_3$, opal, and lithogenic particles from aeolian dust, and an excess POC component, which is approximately restricted to the upper 1,000 m. Thus, fluxes of POC below 1,000 m are mostly bound to minerals, whereby the $CaCO_3$-associated component dominates and contributes to >80% of the total flux (Fig. 1*B*).

Anthropogenic CO_2 Forcing. Imposing anthropogenic emissions at rates depicted in Fig. 2*A* entails an accumulation of CO_2 in the atmosphere, which leads to rising pCO_2 levels up to 1,750 μatm in the year 2200 (Fig. 2*E*). Subsequently, CO_2 levels descend during the emission-free era to 1,400 μatm in the year 3000 (Fig. 2*E*). As a consequence, the globally averaged sea surface pH value drops from 8.15 in 1800 to 7.45 in 2200, relaxing to a value of 7.6 in year 3000. In accord with descending pH values, the sea surface $[CO_3^{2-}]$ and, hence, Ω_{CaCO_3} decrease (Fig. 1*A*), resulting in a drop of the $CaCO_3$/POC export ratio by >75% by the year 2200. Reduced export of $CaCO_3$ diminishes the ballast-bound export flux of POC (F_{CaCO_3}) into the abyssal ocean tremendously. Below 1,000 m, the global mean export of POC (F_{OC}) is reduced by >70% (Fig. 1*B*).

The increase in sea surface temperature (SST) (Fig. 2*B*) results in a higher stratification of the upper ocean, causing a reduced ventilation of the deep ocean and a weakening of the global export production by the year 2100 (Fig. 2*D*). The maximum strength of the AMOC weakens from 23 to 12 Sv by the year 2100. Subsequently, because of a northward shift of the deep-water formation sites, the AMOC grows back to its preindustrial strength by the year 2400. This strengthening of the AMOC is accompanied by a recovery of the global export production. In case of experiment **BALLAST**, its preindustrial value of 8.6 Pg C y^{-1} is even exceeded by ≈15% (see Fig. 2*D*).

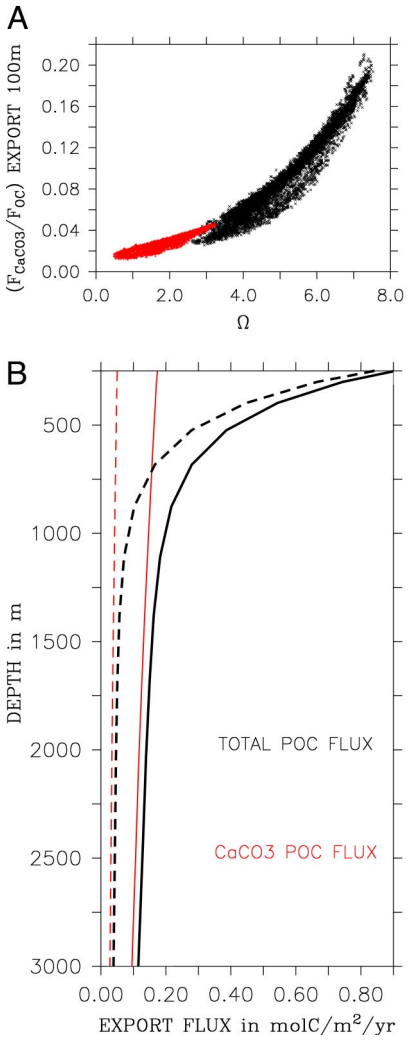

Fig. 1. Carbonate saturation state and export fluxes of POC. (*A*) In situ saturation of sea surface CO_3^{2-} ($\Omega'CaCO_3$) versus F_{CaCO_3}/F_{OC}; black dots, preindustrial relationship; red dots, distribution in the year 2300. (*B*) Profile of the export fluxes of different POC compartments in mol C m $^{-2}$ y^{-1} between 250 and 3,000 m. Black solid line, preindustrial total export flux of POC (F_{OC}); black dashed line, F_{OC} in the year 2300; red solid line, preindustrial export of $CaCO_3$-bound POC; red dashed line, export of $CaCO_3$-bound POC in year 2200.

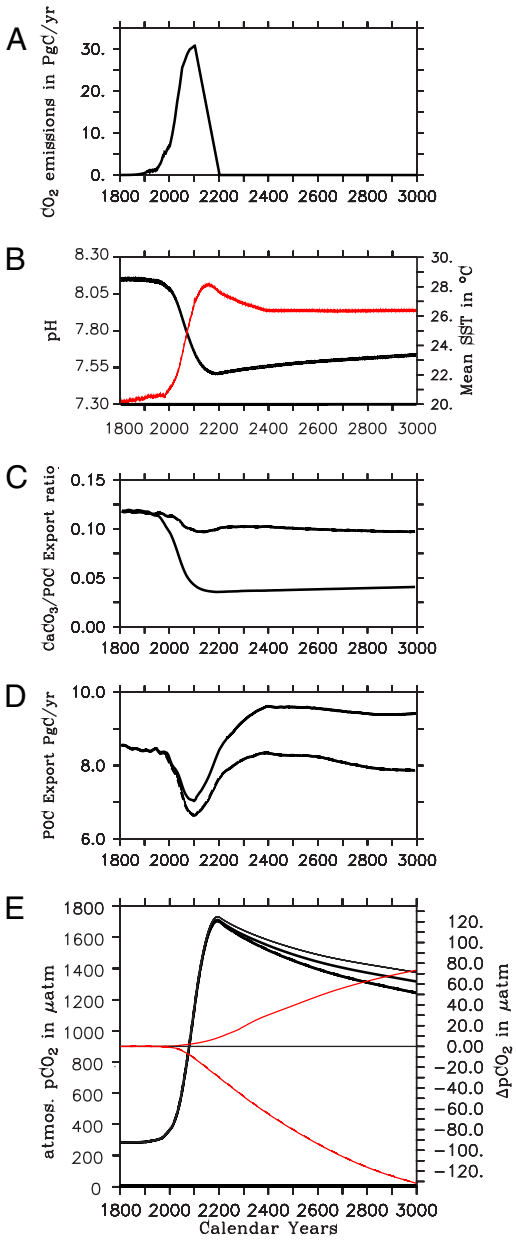

Fig. 2. Time series of imposed anthropogenic CO_2 emissions in Pg C y^{-1} (*A*); global mean sea surface pH value (black) and global mean SST (red) (*B*); $CaCO_3$/POC export ratio after FROZEN_CALC&BALL (dashed line) and BALLAST (solid line) (*C*); POC export in Pg C y^{-1} after BALLAST (solid line) and FROZEN_BALL (dashed line) (*D*); atmospheric pCO_2 levels after FROZEN_CALC&BALL (thin solid line), BALLAST (solid line), and FROZEN_BALL (dashed line) (*E*). Upper red curve, ballast effect ΔpCO_2 (BALLAST-FROZEN_BALL); lower red curve, calcification effect ΔpCO_2 (FROZEN_BALL -FROZEN_CALC&BALL).

The latter can be explained by the fact that, at the expense of the ballasted POC flux, the excess flux of POC (F^E_{OC}) increases. Because the penetration depth of excess POC is much shallower than that of ballasted POC, a relative increase in the amount of detritus accumulating in the subsurface and at intermediate ocean depth leads to an accelerated remineralization. Accordingly, released nutrients will become available to the euphotic zone by upwelling and mixing on a shorter time scale, i.e., the turnover time of the nutrient cycle shortens, resulting in an amplification of the net primary and export production.

Calcification Feedback. To assess the overall effects of the attenuation of biogenic calcification, the 2 model runs **FROZEN_CALC&BALL** and **FROZEN_BALL** (see *Numerical Experiments*, above), imposing the same anthropogenic forcing as in **BALLAST**, have been performed. Although in both experiments (**FROZEN_CALC&BALL** and **FROZEN_BALL**), the response of the $CaCO_3$-bound POC flux on rising pCO_2 levels is neglected, in **FROZEN_CALC&BALL,** additionally the $CaCO_3$/POC export flux ratio is frozen at preindustrial levels. In both experiments, the atmospheric pCO_2 attains a similar high value of ≈1,750 μatm in the year 2200 as in **BALLAST**, but approaches 1,450 μatm in **FROZEN_CALC&BALL** at the end of the simulation (see Fig. 2*E*), whereas in **FROZEN_BALL**, the atmospheric pCO_2 reaches a level of only 1,325 μatm by the end of this millennium. The final value in experiment **FROZEN_CALC&BALL**, which is 125 μatm higher compared with **FROZEN_BALL**, can be explained by the production of CO_2 during the calcification process, which, in contrast to **FROZEN_BALL**, remains at its high preindustrial level until the year 3000. Hence, reduced biogenic calcification caused by rising pCO_2 levels mediates a negative-feedback mechanism. The magnitude of the response of atmospheric pCO_2 values is comparable with recent model studies (29).

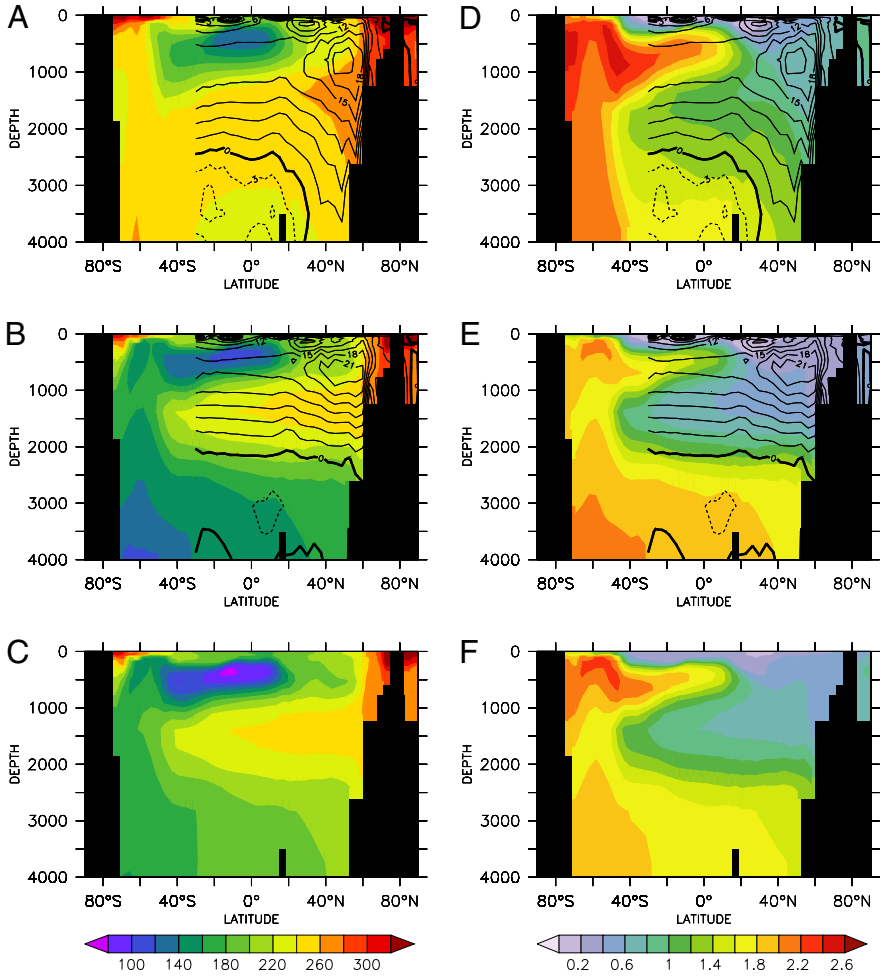

Fig. 3. Atlantic section along 21° W. (*A*) Color, preindustrial dissolved oxygen concentration in μmol L^{-1}; contours, preindustrial AMOC stream function north of 30° S in Sv. The contour interval is 3 Sv. (*B*) Color, O_2 concentration at the end of the millennium without accounting for the ballast effect (experiment FROZEN_BALL); contours, AMOC stream function north of 30° S at the end of the millennium. The contour interval is 3 Sv. Although the maximum overturning strength of the AMOC is comparable with preindustrial values, the inflow of AABW into the Atlantic Ocean is reduced to almost zero. This is mainly caused by the increased melting rate of the Antarctic ice shelf under global warming. Employing the parameterization given in ref. 37 provides a melting rate of ≈147 mSv (1 mSv = 10^3 m^3s^{-1}) by the end of the millennium. This is ≈5 times the preindustrial melting rate provided by the model. (*C*) O_2 concentrations employing the full-scale biogeochemistry model BALLAST at the end of the millennium. The ballast effect increases the hypoxia at the equator between 200 and 800 m in comparison with *B* by lowering the O_2 concentrations by ≈30 μmol L^{-1}. (*D*) Same as in *A* but for phosphate. (*E*) Same as in *B* but for phosphate. (*F*) Same as in *C* but for phosphate. Units are μmol L^{-1}.

Ballast Feedback. The effect of the positive ballast feedback has been inferred from the comparison of experiments **BALLAST** and **FROZEN_BALL**. In case of **FROZEN_BALL** under anthropogenic CO_2 emissions, the atmospheric pCO_2 level rises to nearly the same value by year 2200 as in case of **BALLAST** (see *Anthropogenic CO_2 Forcing*, above), however, as mentioned above, reaching a lower level of 1,325 μatm by the end of this millennium. The small but significant difference of 75 μatm between **BALLAST** and **FROZEN_BALL** in the year 3000 (see Fig. 2*E*) can be explained as follows: According to Eq. **2**, biogenic calcification, and hence $CaCO_3$ export, is reduced by 75% in both experiments at the maximum pCO_2 level projected to be attained in the year 2200. In contrast to **FROZEN_BALL**, in experiment **BALLAST**, the vertical export of deeply sinking $CaCO_3$-bound POC weakens as $[CO_3^{2-}]$ decreases in the mixed layer. As a result, POC accumulates and is oxidized at shallower depth, leading to a change in the vertical profile of DIC toward slightly higher values in the upper ocean combined with increased pCO_2 values at the sea surface. Hence, the reduced flux of $CaCO_3$ under a more acid environment mediates a positive feedback on rising atmospheric pCO_2 levels. Although in experiment **BALLAST**, the export production increases after the year 2300 under high CO_2 conditions compared with preindustrial values by 15%, the reduced availability of mineral ballast entails a weakened marine biological carbon pump.

According to our model setup, the net effect of oceanic acidification on atmospheric pCO_2 is the sum of a reduction of the atmospheric pCO_2 due to the negative calcification feedback and an increase of pCO_2 due to the positive ballast feedback. Hence, we are left with a net reduction of only 50 μatm instead of the 125 μatm when not accounting for the positive CO_2-ballast feedback at the end of the current millennium.

Global Warming and Ocean Hypoxia. As SSTs rise under elevated atmospheric greenhouse gas concentrations (Fig. 2*B*), the solubility of oxygen will decline remarkably (14). Moreover, the increased upper-ocean stratification due to rising temperatures will weaken the deep-ocean ventilation (31). Deep and intermediate water mass formations, mostly occurring in polar and subpolar regions, are regarded as the main processes conveying oxygen from the sea surface down to the ocean's interior, whereas oxidation of sinking POC decreases the oxygen content in the water column. As a result, oxygen-depleted zones can mostly be found underneath zones of high biological production such as the equatorial upwelling areas in the Pacific and Atlantic Oceans at depths of between 200 and 800 m (Fig. 3*A*).

In our model, under preindustrial and present-day conditions, Antarctic Bottom Water (AABW) is mostly formed by sporadic convection events during the austral winter in the Weddell Sea Gyre. Antarctic Intermediate Water (AAIW) forms by mixing and subduction processes at various places in the Southern Ocean between the Subantarctic and Antarctic Polar Front. The North Atlantic Deep Water (NADW) is formed by deep convection in the Nordic Seas and the Labrador Sea.

Given that future anthropogenic CO_2 emissions will follow the SRES A1FI path, the North Atlantic overturning will become reduced by ≈50% between the years 2100 and 2300, although recovering to its initial strength by the year 2400. AABW and AAIW formation, however, will rapidly become inhibited in the

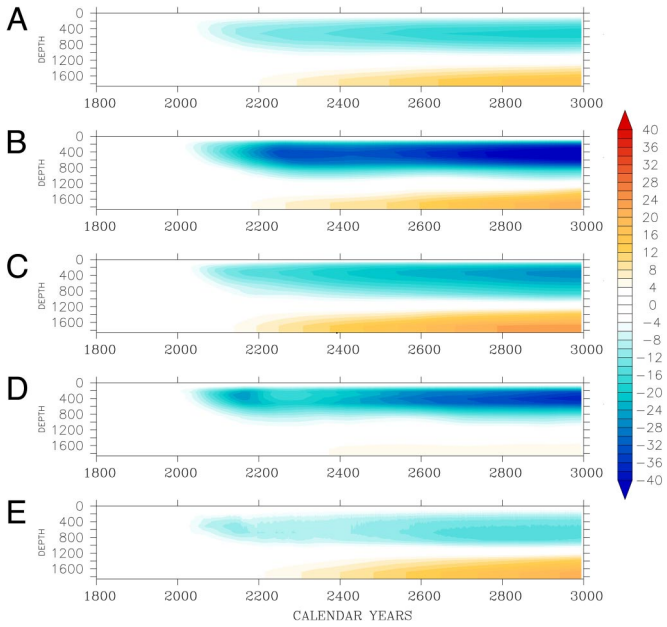

Fig. 4. Hovmöller diagram of the change in averaged oxygen concentrations caused by the ballast effect (BALLAST-FROZEN_BALL). (*A*) Global average. (*B*) Indian Ocean between the equator and 30° N. (*C*) The Atlantic Ocean between 20° S and 20° N and between 20° W and 10° E. (*D*) Pacific Ocean between 20° S and 20° N and between 150° W and 80° W. (*E*) North Pacific Ocean between 40° N and 70° N and between 140° E and 120° W.

post-2100 years, causing a steady deoxygenation of deep and intermediate waters in the ocean until the year 3000. Hypoxic conditions, defined by dissolved oxygen concentrations dropping below 60 to 120 μmol L^{-1} (32), will become more extended in a globally warming ocean (Fig. 3*B*). Because hypoxia exerts stress on macroorganisms, it is likely that this process will provoke an increase of their mortality.

Mineral Ballast and Hypoxia. Besides the physical processes mentioned above, increased oxidation due to either enhanced biological productivity or a shift toward a shallower penetration of sinking POC could also lead to an enhanced deoxygenation of the ocean's water masses at intermediate depth. Results from our experiments reveal, that owing to the inhibited export of POC carried by $CaCO_3$ particles (Fig. 1*B*), excess POC accumulates and oxidizes more intensely at shallow and intermediate water depths between 200 and 800 m in experiment **BALLAST** than in **FROZEN_BALL**, when anthropogenic CO_2 emissions are imposed. As a consequence, both the oxygen consumption (Fig. 3*C*) and the release of nutrients (Fig. 3*F*) in these zones increases accordingly. Fig. 3*C* depicts the resulting oxygen concentration along a section at 21° W in the Atlantic Ocean in the year 3000 when the ballast effect is included. The ballast effect on oxygen along this Atlantic section is most pronounced at the equator at a depth of ≈400 m where oxygen concentrations drop below 80 μmol L^{-1}. In the Arabian Sea, the ballast-induced reduction in oxygen concentrations at a depth level of 500 m even exceeds 50 μmol L^{-1} (see Fig. S2).

A Hovmöller diagram of the oceanic evolution of deoxygenation in several parts of the ocean solely owing to the mineral ballast effect (**BALLAST–FROZEN_BALL**) between the years 1800 and 3000 is shown in Fig. 4. Below 1,000 m, the ballast effect acts in the opposite direction and drives oxygen concentrations toward slightly higher values, which is a consequence of the reduced oxidation rates (Fig. 4).

A recent compilation of data (32) reveals an expansion of the oxygen-depleted layer between 300 m and 700 m depth during the last 50 years and declining oxygen concentrations therein at a rate between 0.09 and 0.34 μ mol kg^{-1} y^{-1}. Experiment **BALLAST** provides comparable values of ≈0.2 to 0.5 μmol kg^{-1} y^{-1} averaged over the water column between 300 and 700 m for the same period in the upwelling area off Peru and the Western Subarctic Pacific, respectively.

Summary. Although peaking at 1,750 μatm in the year 2200, the atmospheric concentration of CO_2 is projected to reach values of ≈1,400 μatm at the end of our millennium. Acidification of the upper ocean owing to rising atmospheric CO_2 levels within the current millennium, imposed by a business-as-usual emission path, will not only inhibit the formation of calcareous skeletons by planktonic organisms but also affect atmospheric CO_2 concentrations via a combination of negative and positive feedbacks. Biogenic formation of $CaCO_3$, is associated with a release of CO_2. Hence, a reduction of calcification under rising CO_2 levels exerts a negative feedback toward a stabilization of the Earth climate. In our model studies, the negative calcification feedback entails lower atmospheric pCO_2 values by 125 μatm by the end of the current millennium.

The inclusion of the mineral ballast effect as parameterized in ref.16 allows us to assess the impact of a reduction of deep sinking POC due to a shortage in the $CaCO_3$ production, equivalent to a weakening of the marine biological carbon pump. Here, we can show that the response of atmospheric pCO_2 values due to a weaker biological carbon pump is an increase of ≈75 μatm by the end of this millennium—the positive ballast feedback. Consequently, the negative calcification feedback will become reduced by ≈60%. Our simulations give an example of the "intricate dynamic adjustment and feedback processes" in the marine carbon cycle as mentioned in ref. 33. Moreover, in light of ref. 30, one could speculate about biogenic calcification as being a "tipping element" in the climate system.

The most striking impact of a reduced mineral ballast export was found in the decline of oxygen concentrations in oceanic zones located at depth between 200 and 800 m. In the Equatorial Atlantic at 21° W, the ballast effect will reduce oxygen concentrations by ≈30 μmol L^{-1} at 400-m depth by the year 3000. In the Arabian Sea at 500-m depths, a reduction of the dissolved oxygen concentration of >50 μmol L^{-1}, is projected to occur at the end of this millennium. Accelerated remineralization of POC at shallower depth, a consequence of the acidification-induced inhibition of the mineral ballast flux, ultimately tends to expand hypoxic zones in the ocean, which will have negative impacts on the marine ecosystems by possibly increasing the mortality of marine organisms. Our study indicates that unbridled ocean acidification would exacerbate the observed hypoxia trends due to various environmental factors as reported in recent empirical studies.

Methods

Ocean Physics. The physical model used in the current study is an ocean–sea ice general circulation model based on MOM-3, which was coupled to an anomaly model of the atmospheric energy–moisture balance (34). The latter was constructed to account for small deviations from a given atmospheric climatology, allowing for simulating ocean–atmosphere feedback mechanisms. The atmospheric forcing has to be provided externally. Here, we use the NCEP/NCAR reanalysis database (35). The spatial resolution of the current model setup is slightly coarser then in the standard version (34) with a horizontal mesh size of 3.75° × 3.75° and 24 vertical levels with thickness increasing from 25 m at the top to 500 m at the bottom. The model includes an empirical parameterization of bottom-enhanced vertical mixing similar to that of ref. 36, with a vertical background diffusivity of 0.1 cm^2 s^{-1}. Isopycnic Redi stirring was set to 1.25×10^7 cm^2 s^{-1}, whereas thickness diffusivities vary between 0.275 and 0.55×10^7 cm^2 s^{-1}. Ice shelf melting around Antarctica is parameterized according to ref. 37. The OGCM benefits from a second-order moments advection scheme invented by ref. 38, which is nearly free of spurious diffusion and dispersion (34).

Biogeochemistry. The biogeochemistry submodel, coupled to the MOM-3 code, was developed on the basis of the HAMOCC-3.1 code [Six and Maier-Reimer (39)] and comprises the following prognostic ocean tracers: dissolved inorganic carbon (DIC), total alkalinity (ALKA), phosphate (PO_4), oxygen (O_2), phytoplankton

(PHY), zooplankton (ZOO), particulate organic carbon (POC), particulate inorganic carbon ($CaCO_3$), and dissolved organic carbon (DOC). In addition to this configuration, we have implemented models of the silicate ($SiOH_4$), nitrate (NO_3), and iron (Fe) cycle. The $SiOH_4$ model was adapted from ref. 40, whereas the NO_3 cycle was implemented according to ref. 41. Based on observations, which have been discussed in ref. 40, the biogenic opal-to-carbon export ratio ($\frac{Si}{C}$) is assumed to depend on the ambient $SiOH_4$ and dissolved Fe concentration, which is larger for high [$SiOH_4$] and low [Fe] conditions and vice versa. The model accounts for denitrification in regions with O_2 concentrations <10 μmol L^{-1} and parameterizes nitrogen fixation in the ocean surface by simply restoring the NO_3 concentrations toward the $P/N = 1{:}16$ Redfield stoichiometry. The iron cycle model was adopted from Parekh *et al.* (42, 43), where a uniformly distributed organic ligand (44) prevents dissolved iron from becoming scavenged and precipitated within the water column and permits the simulation of realistic iron concentrations in the ocean. Aeolian dust fluxes, imposed from simulations with the GISS atmospheric model (45), have been assumed to be the only source of dissolved iron. For numerical simplicity, the Fe/C ratio during biological uptake, export, and remineralization is kept at a mean community value of 5 μmol L^{-1}/1 mol L^{-1} (46).

The growths rates of phytoplankton have been parameterized as a function of photosynthetically available radiation (PAR), temperature, mixed layer depth, and the concentrations of micro and macro nutrients, where only the scarcest nutrient available is regarded to be the limiting factor (Liebigs law). The biogeochemistry model is isogeochemical, i.e., chemical weathering and exchange processes with the oceanic sediment are not included.

The steady-state vertical distribution $F_i(z)$ of the export flux of POC and mineral ballast below 100 m is calculated according to

$$F_i(z) = F_i(100\ \mathrm{m}) \cdot \exp\{-(z - 100\ \mathrm{m})/z_{p_i}\},$$

where z_{pi} is the e-folding penetration depth of the compartment i in meters, which was chosen such that the globally averaged shape of $F_{OC}(z)$ (see Eq. **1**) resembles the Martin curve (47).

Air–sea gas transfer coefficients are taken from ref. 48, and CO_2 solubility and the carbonate system equilibrium constants are taken from ref. 49. The coupled ocean–sea ice–atmosphere-biogeochemistry model is referred to as POTSMOM-C.

Anthropogenic Forcing. Because POTSMOM-C includes an anomaly model of the atmospheric energy–moisture balance (for details see ref. 34), which is applicable only when accounting for the effects of small deviations from a given climatology, the transient response of atmospheric variables on elevated CO_2 levels, such as surface temperature, relative humidity, and precipitation, have to be imposed from a climate model. Here, we use results from a climate projection by employing CLIMBER-3α (31), which has followed the same anthropogenic emission path between the years 1800 and 2400 as in the present study. Because the CLIMBER-3α simulation ends in 2400 AD, we continue to apply the atmospheric anomalies from this last model year to the subsequent years until 3000 AD. Therefore, the atmospheric anomalies between years 2400 and 3000 have to be regarded as an upper bound.

ACKNOWLEDGMENTS. We thank Stefan Rahmstorf, David Archer, and Dieter Wolf–Gladrow for constructive comments and helpful discussions. This work was supported by the German ''Pakt für die Forschung,'' which is funding the project ''Tipping Point Interactions (TIPI).''

1. Key RM, *et al.* (2004) A global ocean carbon climatology: Results from Global Data Analysis Project (GLODAP). *Global Biogeochem Cycles* 10.1029/2004GB002247.
2. Schlitzer R (2000) Electronic atlas of WOCE hydrographic and tracer data now available. *Eos Trans AGU* 81(5):45.
3. Sabine CL, *et al.* (2004) The oceanic sink for anthropogenic CO_2. *Science* 305:628–633.
4. Orr JC, *et al.* (2005) Anthropogenic ocean acidification over the twenty-first century and its impact on calcifying organisms. *Nature* 437:681–686.
5. Kleypas JA, *et al.* (1999) Geochemical consequences of increased atmospheric carbon dioxide on coral reefs. *Science* 284:118.
6. Riebesell U, *et al.* (2000) Reduced calcification of marine plankton in response to increased atmospheric CO_2. *Nature* 407:364–367.
7. Zondervan I, Zeebe RE, Rost B, Riebesell U (2001) Decreasing marine biogenic calcification: A negative feedback on rising atmospheric CO_2. *Global Biogeochem Cycles* 15:507–516.
8. Delille B, *et al.* (2005) Response of primary production and calcification to changes of pCO_2 during experimental blooms of the coccolithophorid *Emiliania huxleyi*. *Global Biogeochem Cycles* 10.1029/2004GB002318.
9. Wolf-Gladrow DA, Riebesell U, Burkhardt S, Bijma J (1999) Direct effects of CO_2 concentration on growth and isotopic composition of marine plankton. *Tellus B* 51:461–476.
10. Iglesias-Rodriguez MD, *et al.* (2008) Phytoplankton calcification in a high-CO_2 world. *Science* 320:336–340.
11. Iglesias-Rodriguez MD, *et al.* (2008) Response to comment on ''Phytoplankton calcification in a high-CO_2 world''. *Science* 322:1466.
12. Riebesell U, *et al.* (2008) Comment on ''Phytoplankton calcification in a high-CO_2 world''. *Science* 322:1466.
13. Volk T, Hoffert MI (1985) The carbon cycle and atmospheric CO_2: Natural variations Archean to present. *Geophys Monogr Ser*, eds Sundquist ET, Broecker WS (American Geophysical Union, Washington, DC), Vol. 32, pp 99–111.
14. Broecker WS, Peng TH (1982) *Tracers in the Sea* (Eldigo, Palisades, NJ).
15. Frankignoulle M, Canon C, Gattuso JP (1994) Marine calcification as a source of carbon dioxide: Positive feedback of increasing atmospheric CO_2. *Limnol Oceanogr* 39:458–462.
16. Klaas C, Archer DE (2002) Association of sinking organic matter with various types of mineral ballast in the deep sea: Implications for the rain ratio. *Global Biogeochem Cycle* 10.1029/2001GB001765.
17. Armstrong RA, Lee C, Hedges JI, Hinjo S, Wakeham SG (2002) A new, mechanistic model for organic carbon fluxes in the ocean based on the quantitative association of POC with ballast minerals. *Deep Sea Res II* 49:219–236.
18. Howard MT, Winguth AME, Klaas C, Maier-Reimer E (2005) Sensitivity of ocean carbon tracer distributions to particulate organic flux parameterizations. *Global Biogeochem Cycles* 10.1029/2005GB002499.
19. Gehlen M, *et al.* (2006) Reconciling surface ocean productivity, export fluxes and sediment composition in a global biogeochemical ocean model. *BioGeosciences* 3:521–537.
20. Barker S, Higgins JA, Elderfield H (2003) The future of the carbon cycle: Review, calcification response, ballast and feedback on atmospheric CO_2. *Phil Trans R Soc London* 361:1977–1999.
21. Mucci A (1983) The solubility of calcite and aragonite in seawater at various salinities, temperatures and on atmospheric total pressure. *Am J Sci* 283:780–799.
22. Marland G, Boden TA, Andres RJ (2007) Global, regional, and national fossil fuel CO_2 emissions. *Trends: A Compendium of Data on Global Change* (Carbon Dioxide Information Analysis Center, Oak Ridge National Laboratory, US Department of Energy, Oak Ridge, TN), Tech Rep.
23. Nakićenović N, Swart R (2000) *IPCC Special Report on Emissions Scenarios* (Cambridge Univ Press, Cambridge, UK).
24. Schneider B, *et al.* (2008) Climate-induced interannual variability of marine primary and export production in three global coupled climate carbon cycle models. *BioGeosciences* 5:597–614.
25. Najjar RG, *et al.* (2007) Impact of circulation on export production, dissolved organic matter, and dissolved oxygen in the ocean: Results from phase II of the ocean carbon-cycle model intercomparison project (OCMIP-2). *Global Biogeochem Cycles* 10.1029/2006GB002857.
26. Matsumoto K, Sarmiento JL, *et al.* (2004) Evaluation of ocean carbon cycle models with data-based metrics. *Geophys Res Lett* 10.1029/2003GL018970.
27. Jin X, Gruber N, Dunne JP, Sarmiento JL, Armstrong RA (2006) Diagnosing the contribution of phytoplankton functional groups to the production and export of particulate organic carbon, $caco_3$, and opal from global nutrient and alkalinity distributions. *Global Biogeochem Cycles* 10.1029/2005GB002532.
28. Sarmiento JL, *et al.* (2002) A new estimate of the $CaCO_3$ to organic carbon export ratio. *Global Biogeochem Cycles* 10.1029/2002GB001919.
29. Ridgewell A, Zondervan I, Hargreaves JC, Bijma J, Lenton TM (2007) Assessing the potential long-term increase of oceanic fossil fuel CO_2 uptake due to CO_2-calcification feedback. *BioGeosciences* 4:481–492.
30. Lenton TM, *et al.* (2008) Tipping elements in the Earth's climate system. *Proc Natl Acad Sci USA* 105:1786–1793.
31. Kuhlbrodt T, *et al.* (2008) An integrated assessment of changes in the thermohaline circulation. submitted. *submitted to Climatic Change*.
32. Stramma L, Johnson GC, Sprintall J, Mohrholz V (2008) Expanding oxygen-minimum zones in the tropical oceans. *Science* 320:655–658.
33. Schellnhuber HJ (2008) Global warming: Stop worrying, start panicking? *Proc Natl Acad Sci USA* 105:14239–14240.
34. Hofmann M, Maqueda MAM (2006) Performance of a second-order moments advection scheme in an ocean general circulation model. *J Geophys Res* 10.1029/2005JC003279.
35. Kalnay E, *et al.* (1996) The NCEP/NCAR 40-years reanalysis project. *Bull Am Meteorol Soc* 77:437–471.
36. Hasumi H, Suginohara N (1999) Effects of locally enhanced vertical diffusivity over rough bathymetry on the world ocean circulation. *J Geophys Res* 104:367–374.
37. Beckmann A, Goosse H (2003) A parameterization of ice shelf–ocean interaction for climate models. *Ocean Modelling* 5:157–170.
38. Prather MJ (1986) Numerical advection by conservation of second-order moments. *J Geophys Res* 91:6671–6681.
39. Six K, Maier-Reimer E (1996) Effects of phytoplankton on seasonal carbon fluxes in an ocean general circulation model. *Global Biogeochem Cycles* 10:559–583.
40. Aumont O, Maier-Reimer E, Blain S, Monfray P (2003) An ecosystem model of the global ocean including Fe, Si, P colimitations. *Global Biogeochem Cycles* 10.1029/2001GB001745.
41. Maier-Reimer E, Kriest I, Segschneider J, Wetzel P (2005) The Hamburg Ocean Carbon Cycle Model HAMOCC5.1—Technical description release 1.1. *Reports on Earth Systems Science 14*, (MPI, Hamburg, Germany), Tech Rep.
42. Parekh P, Follows MJ, Boyle EA (2004) Modeling the global ocean iron cycle. *Global Biogeochem Cycles* 10.1029/2003GB002061.
43. Parekh P, Follows MJ, Boyle EA (2005) Decoupling of iron and phosphate in the global ocean. *Global Biogeochem Cycles* 10.1029/2004GB002280.
44. Archer D, Johnson K (2000) A model of the iron cycle in the ocean. *Global Biogeochem Cycles* 14:269–279.
45. Tegen I, Fung I (1995) Contribution to the atmospheric mineral aerosol load from land surface modification. *J Geophys Res* 100:18707–18726.
46. Sunda WG, Huntsman SA (1995) Iron uptake and growth limitation in oceanic and coastal phytoplankton. *Mar Chem* 50:189–206.
47. Martin JH, Knauer GA, Karl DM, Broenkow WW (1987) VERTEX: Carbon cycling in the North Pacific. *Deep Sea Res A* 34:267–285.
48. Wanninkhof R (1992) Relationship between wind speed and gas exchange over the ocean. *J Geophys Res* 97:7373–7382.
49. DOE (1994) eds, Dickson A, Goyet C (ORNL/CDIAC-74).